

Supporting Information

Wide-temperature-range multispectral camouflage enabled by orientation–gradient co-optimized microwave blackbody metastructure coupled with conformal MXene coating

Li Yao ^a, Longkai Pan ^a, Shixiang Zhou ^{a,b}, Hongxia Liu ^a, Hui Mei ^{a,*}, Yang Li ^c, Konstantinos G. Dassios ^d, Paolo Colombo ^{e,f}, Laifei Cheng ^a, Litong Zhang ^a

^a *Science and technology on Thermostructural Composite Materials Laboratory, School of Materials Science and Engineering, Northwestern Polytechnical University, Xi'an Shaanxi 710072, PR China*

^b *Department of Materials Science and Engineering, National University of Singapore, 9 Engineering Drive 1, Singapore 117576, Singapore*

^c *National Key Laboratory of Science and Technology on High-strength Structural Materials, Central South University, Changsha 410083, China*

^d *Department of Chemical Engineering, University of Patras, Karatheodory 1, Patras 26504, Greece*

^e *Department of Industrial Engineering, University of Padova, Padova 35131, Italy*

^f *Department of Materials Science and Engineering, The Pennsylvania State University, University Park, PA 16802, USA*

* Corresponding author. Tel.: +86-29-88495312; fax: +86-29-88494620.

Contents

Supporting Note 1: GA-empowered Gradient Optimization of GGS architecture	3
Supporting Note 2: Experimental Section.....	4
Supplemental Figures.....	9
Supplemental Tables	15
References	17

Supporting Note 1: GA-empowered Gradient Optimization of GGS architecture

Here, we resort to the genetic algorithm (GA) to optimize the GGS's gradient through CST-MATLAB co-simulation. All operations, including modeling, simulations, and parameter modification, were carried out directly in MATLAB, which can make full use of the data processing capabilities of MATLAB and of the electromagnetic computing capabilities of the commercial CST Microwave Studio[®] tool. As shown in Fig. 1b, a finite element discretization approach is used to simplify the complex-shaped GGS110 model, and the genetic algorithm is used to optimize the $|c|$ curvature. Referring to Zhu's works^{1, 2}, the relationship curves of $|c|$ versus z (i.e., $c(z)$) can be regressed by the following cubic polynomial as follows:

$$c(z) = Az^3 + Bz^2 + Cz + D \quad (S1)$$

where parameters of $[A, B, C, D]$ directly determine $|c|$ curvature, thus regulating the GGS's impedance characteristics. Good microwave absorption performance necessitates a balance between low reflection and strong absorption properties, so the objective function is set as follows:

$$\min F(x) = -w_1 * \text{mean}(\alpha_{\text{MW}}) / 0.90 + w_2 * \text{max}(\rho_{\text{MW}}) / 0.10 \quad (S2)$$

$$\text{subject to: } X = \{A, B, C, D\} \in \{[-1, 1], [-1, 1], [-1, 1], [-1, 1]\} \quad (S3)$$

$$w_1 + w_2 = 1 \quad (S4)$$

where microwave response of α_{MW} and ρ_{MW} can be provided by the simulation in CST for a GGS architecture with various parameters of $[A, B, C, D]$. w_1 and w_2 are the weight coefficients that can be adjusted according to the requirements. Because our objective requires a balance between low reflection and high absorption, the weight coefficient w_1 is set as 0.90. The optimization objective is close to the microwave absorption capability with an average

absorptivity of greater than 90% and maximum reflectivity of less than 10% under normal incidence. CST is used to obtain the value of the objective function (S2), and the main body of the GA is executed in MATLAB software via using the “ga” function, which can be applied to find the minimum of function (S2) using the genetic algorithm. For identical GGS architectures, the number of constituent cubic voxels, which directly affects the iteration period, is proportional to the third power of the inverse of the voxel edge size. Therefore, as shown in Fig. 1b, the parameter range of $[A, B, C, D]$ can be first quickly reduced using a large voxel edge size ($T/10$) and the resulting optimization parameters can then be inputted as the initial values of subsequent steps. Then the optimal solution of $[A, B, C, D]$ can be obtained by gradually reducing the voxel edge size (from $T/10$ to $T/40$), greatly reducing the computational effort.

During the optimization procedure, the parameters of GA optimization are set as follows: the population size is 50 per generation, the crossover probability is set to 0.8, the mutation rate is set to 0.1, and the number of genetic iterations is set to 400. Finally, as-obtained best individuals are $[0, 0.0844, -0.3595, 0.3897]$, $[0, 0.0812, -0.2877, 0.3049]$ and $[0, 0.0565, -0.2397, 0.3043]$ for GGS110-2.0, -2.5 and 3.0 architecture, respectively, and the related $c(z)$ curves are shown in Fig. 1c.

Supporting Note 2: Experimental Section

2.1 Material Fabrication

Synthesis of $Ti_3C_2T_x$ MXene: Aqueous MXene dispersions were prepared using the previously reported “MILD” method³⁻⁵ and the specific procedure is as follows: First, 0.66 g of LiF was

dissolved in 10 mL of 6 M HCl in a PTFE container and the mixture was stirred to mix thoroughly. Then, 1 g of Ti_3AlC_2 powders were slowly added to react for 24 h at 40°C under continuous stirring, after which the resultant slurry was repeatedly washed with deionized water addition and centrifuged at 3500 rpm until the supernatant reached a pH value ≈ 6 . The $\text{Ti}_3\text{C}_2\text{T}_x$ sediment was redispersed in deionized water, collected after 5 min of centrifugation at 3500 rpm, and dried in a vacuum desiccator at room temperature for 24 h. To completely delaminate $\text{Ti}_3\text{C}_2\text{T}_x$, 0.25 g of freshly produced powders were again mixed with 50 mL of deionized water, bath-sonicated for 1 h under continuous argon (Ar) bubbling to minimize oxidation, and then the resultant dark aqueous MXene dispersions of few-layer $\text{Ti}_3\text{C}_2\text{T}_x$ at a low concentration of 5 mg/mL was obtained for the subsequent spraying process. The free-standing MXene film was fabricated using a simple vacuum-assisted filtration through a $0.22\ \mu\text{m}$ MCE membrane (JINTENG Inc., Tianjin, China) and peeled off from the filter membrane after drying at ambient temperature. All reagents used in the study were of analytical quality and were used in their as-received condition.

Additive Manufacturing of GGS110-structured SiOC: our prior work describes in detail the technique for preparing photocurable high-precision precursor slurries of SiOC.^{6,7} A top-down vat photopolymerization 3D printer (Octave Light R1-30 μm , Dongguan Octave Light Technology Limited) was utilized to fabricate GGS structured green bodies with a printing layer thickness of 30 μm . The STL-format models of GGS metastructure, created by the function of “RegionPlot3D” in Mathematica software according to formulae (1-5), were imported to the printer to produce green bodies (Fig. 2a, orange-colored samples). To obtain the final SiOC

samples (Fig. 2a, black-colored samples), as-printed green bodies were pyrolyzed at different temperatures under nitrogen atmosphere according to the previous work.⁷

Preparation of GGS110 M@SiOC: following published work⁸⁻¹⁰, we fabricated low-emission MXene coatings by spraying an aqueous MXene dispersion onto as-pyrolyzed GGS110-2.0-z_{opt} SiOC substrate using an air spray gun with a 0.5 mm nozzle attached to an air compressor. The spray rate was set to between 0.05 and 0.09 mL/s and the spray gun was moved back and forth across the samples from a height of about 10 cm, which allows for the preparation of uniformly distributed MXene coatings on the SiOC substrate. Then, the final GGS110 M@SiOC samples can be obtained after drying in a vacuum desiccator at room temperature for 24 h.

2.2 Material Characterizations

The phase constituents were identified by X-ray diffraction (XRD; Bruker, D8 Avance, Germany), and SC-MXene, with a silicate glass with dimensions of $2.0 \times 1.0 \times 0.3 \text{ cm}^3$ (as shown in the right-lower part of Fig.4f) as the substrate, was analyzed by grazing incidence XRD with a 3° grazing incidence angle. With good contact with the four-point probe, the same samples of SC-MXene attached to the glass substrate were used to measure the sheet resistance by the four-point probe method using a ST2558B-F01 probe instrument (Suzhou Lattice Electronics Co., Ltd.). Moreover, pre-oxidized SC-MXene samples were prepared by placing them in a muffle furnace and holding them at different temperatures, from 100 to 450°C with an interval of 50°C under air atmosphere for 30 min. X-ray photoelectron spectroscopy (XPS) analyses were used to identify the terminal groups of synthesized $\text{Ti}_3\text{C}_2\text{T}_x$ MXene. The microstructure and micromorphology were examined further using a transmission electron microscope (TEM; Themis Z, FEI, USA) and scanning electron microscopy (SEM; Zeiss,

Sigma 300) equipped with energy-dispersive X-ray spectroscopy (EDS). Atomic force microscopy (AFM; Bruker, Germany) working in the tapping mode was performed to characterize the thickness of monolayer $Ti_3C_2T_x$ MXene. The static contact angle profiles of a SiOC substrate with aqueous MXene dispersions were obtained with a contact angle goniometer (JY-82B, Kruss, DSA). The surface density of the GGS-structured SiOC-based MMBs was calculated as the product of d_{eff} and solid density ρ_0 , where ρ_0 equals 1.698 g/cm^3 according to previous work.⁶

2.3 Electromagnetic Measurement

Microwave response measurement: As shown in Fig. 3a, referring to our previous work⁷, a transmission/reflection method using rectangular waveguides was employed here to characterize the wide-temperature (RT-500°C) microwave response in the X-Ku band using an Anritsu Model MS4644A vector network analyzer. The complex permittivity of solid SiOC samples (Fig. S1a) was also determined using the vector network analyzer, with dimensions of 22.860 mm (length, L) \times 10.160 mm (width, W) in X-band and 15.799 mm (L) \times 7.899 mm (W) in Ku-band, respectively. Experimentally measured S-parameters S_{11} and S_{21} were used to calculate reflectivity (ρ_{MW}), transmissivity (τ_{MW}), and absorptivity (α_{MW}) of samples by $\rho_{\text{MW}} = |S_{11}|^2$, $\tau = |S_{21}|^2$, and $\alpha_{\text{MW}} = 1 - |S_{11}|^2 - |S_{21}|^2$.

IR-VIS measurement: The absorption/emission properties over 3-14 μm were evaluated using a Nicolet iS50 Fourier transform infrared (FTIR) spectrometer equipped with a gold integrating sphere, while the VIS/NIR (0.38-1.2 μm) absorptance spectra were collected using a spectrometer (Lambda 950, Perkin Elmer) equipped with a 150 mm integrating sphere with the reflection of a standard $BaSiO_4$ white plate as reference. At the indoor ambient temperature

($\sim 20^\circ\text{C}$), the radiation temperature was measured with an LWIR camera (FLIR T620) operating at $7.5\text{-}14\ \mu\text{m}$. A heating plate (HTL-300EX, Shenzhen Boda Jingke Biotechnology Co., Ltd, China) was used to mimic camouflaging objects with different temperatures. All samples were placed on the heating plate and held at various temperatures for 20 min, and then their thermal LWIR images were captured. The actual temperature of the heating plate was calibrated by a thermocouple (YET-620) with a K-type microprobe. The bulk M@SiOC , SiOC , and reference BP@SiOC for the IR camouflage testing are with dimensions of $15.0 \times 15.0 \times 1.5\ \text{mm}^3$. Based on the above-mentioned SC-MXene samples attached to the glass substrate for the sheet resistance testing, the LWIR camouflage ability of SC-MXene after pre-oxidation at different temperatures was also characterized by the LWIR camera (FLIR T620) at a fixed temperature of 50°C , which is slightly higher than the room temperature to avoid the interference from the surrounding heat sources such as the human body and the lighting device. The glass substrate in this instance can guarantee a flat SC-MXene profile, preventing surface undulations from affecting the LWIR camouflage performance. Besides, as shown in the left lower part of Fig.4f, a piece of electrical tape (3M Scotch Super 88 Vinyl, with a known emissivity of 0.95^{11}) was adhered to the glass substrate to be used as the reference blackbody, which can reflect the actual surface temperature of the glass substrate (equivalent to SC-MXene coating) by the LWIR imaging and bring out the SC-MXene's LWIR camouflage properties.

2.4 Microwave Electromagnetic Simulation

Referring to our previous work,⁷ the electromagnetic simulation at microwave frequencies was performed using CST by adopting a Frequency Selective Surface metamaterial-unit cell template, with unit cell boundary conditions in both the x - and y -axes directions and Floquet

port excitations along the z -axis. The electromagnetic parameters (Fig. S1a) of solid SiOC pyrolyzed at 1300°C were set as substrate material parameters. The polarization direction was parallel to the y -direction (Fig. 1b). The frequency-domain solver with a hexahedral mesh was adopted. The obtained S parameters were then post-processed to acquire simulated reflectivity, transmissivity, and absorptivity of GGS structures.

2.5 First-Principles Calculations of VIS–IR Reflectivity

With reference to previous works¹²⁻¹⁵, first-principles calculations for VIS-IR reflectivity were implemented using Cambridge Sequential Total Energy Package (CASTEP) based on density functional theory, which is available as a user-friendly module with the material studio software. The Generalized Gradient Approximation (GGA) of the Perdew-Burke-Ernzerhof (PBE) method was used in the approximation of the exchange-correlation part. A OTFG ultrasoft pseudopotential was selected for the optical properties' calculations, and the cut-off energy was set to 571.4 eV. In structural optimization and optical properties calculations, the SCF tolerance was set to a value of 1.0×10^{-6} eV/atom, and the total energy convergence was less than 1.0×10^{-5} eV/atom. The maximum force was taken as 0.03 eV/Å, the maximum stress was less than 0.05 GPa, and the maximum atomic displacement was less than 1×10^{-3} Å.

Supplemental Figures

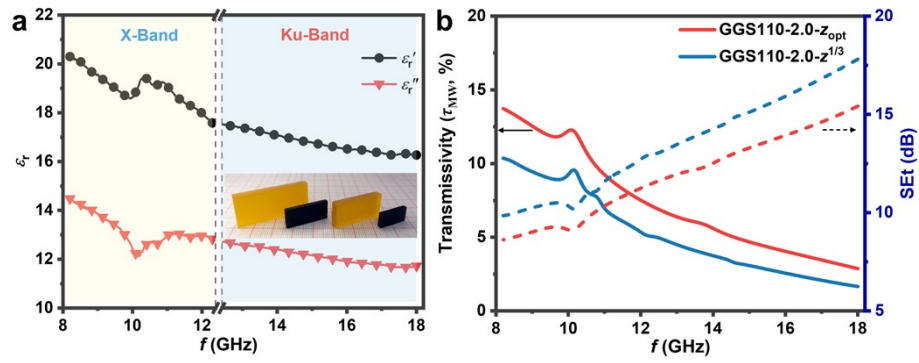


Fig. S1 (a) Experimentally determined complex permittivity in the X-Ku band of solid SiOC pyrolyzed at 1300°C⁷; (b) The simulated frequency dependence of transmissivity (τ_{MW}) for both GGS110-2.0- z_{opt} and $-z^{1/3}$ SiOC MMBs.

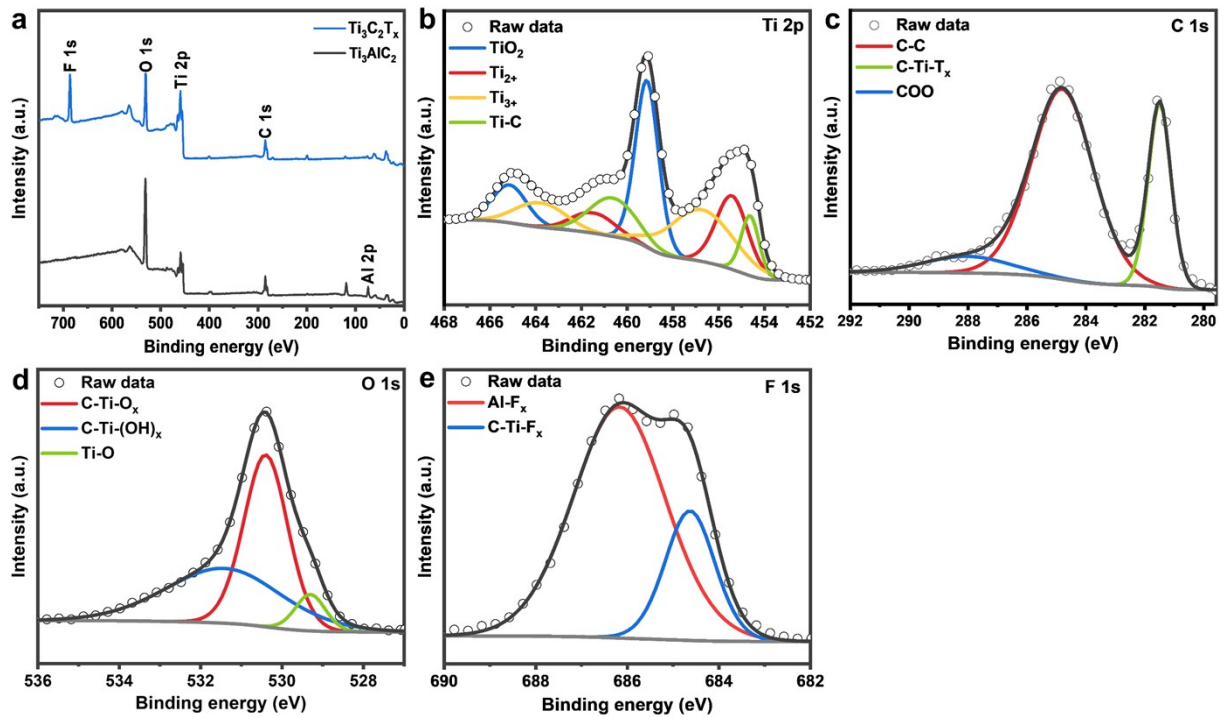


Fig. S2 (a) The survey XPS spectra of as-synthesized $Ti_3C_2T_x$ and raw Ti_3AlC_2 powders. The high-resolution XPS spectra of (b) Ti 2p, (c) C 1s, (d) O 1s, and (e) F 1s for $Ti_3C_2T_x$.

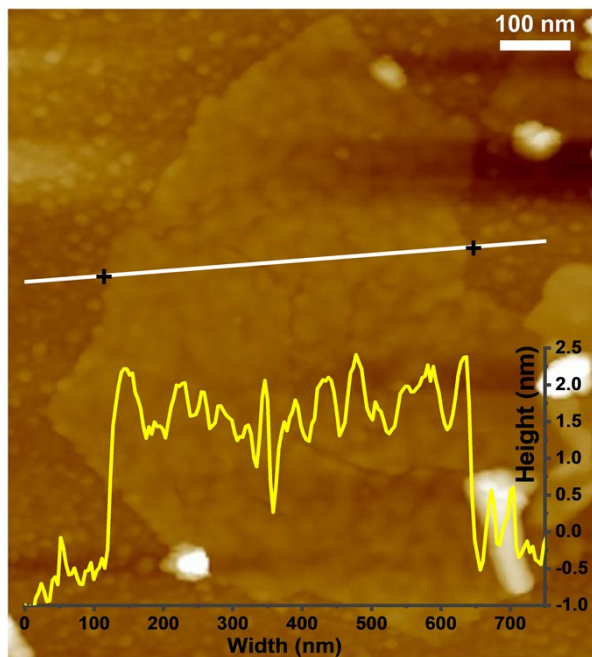


Fig. S3 AFM image of $\text{Ti}_3\text{C}_2\text{T}_x$ nanosheets.

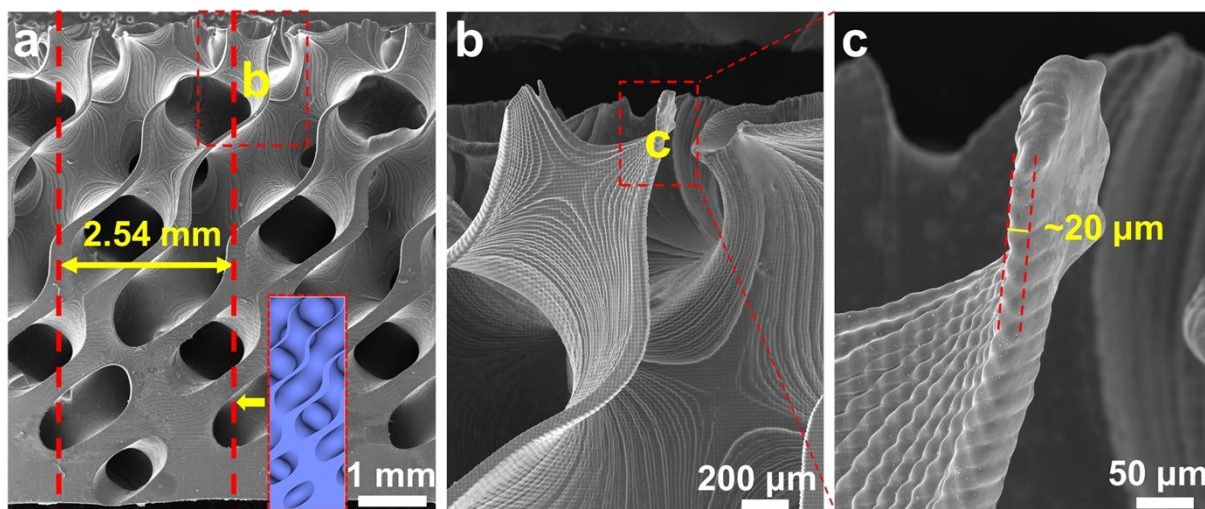


Fig. S4 Another side view of the micromorphology of a GGS110-2.0- z_{opt} M@SiOC specimen at different magnifications.

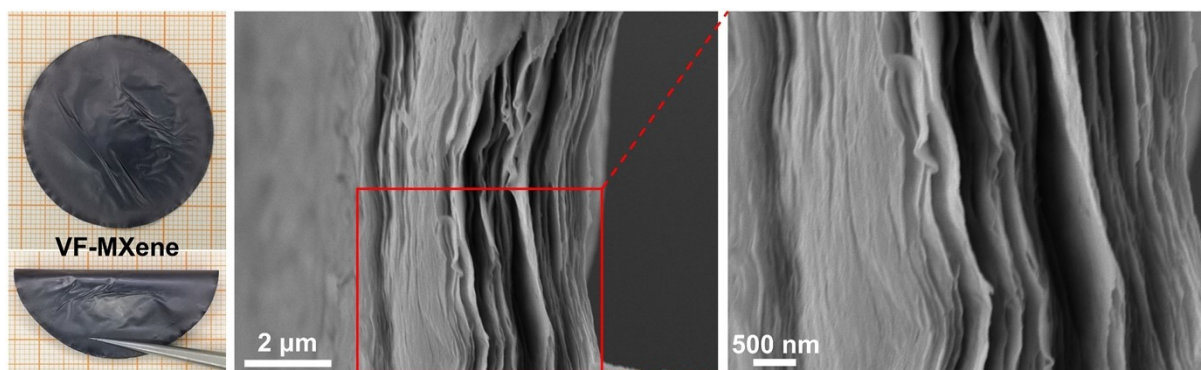


Fig. S5 Optical image and the micromorphology of the fracture surface of a free-standing VF-MXene film.

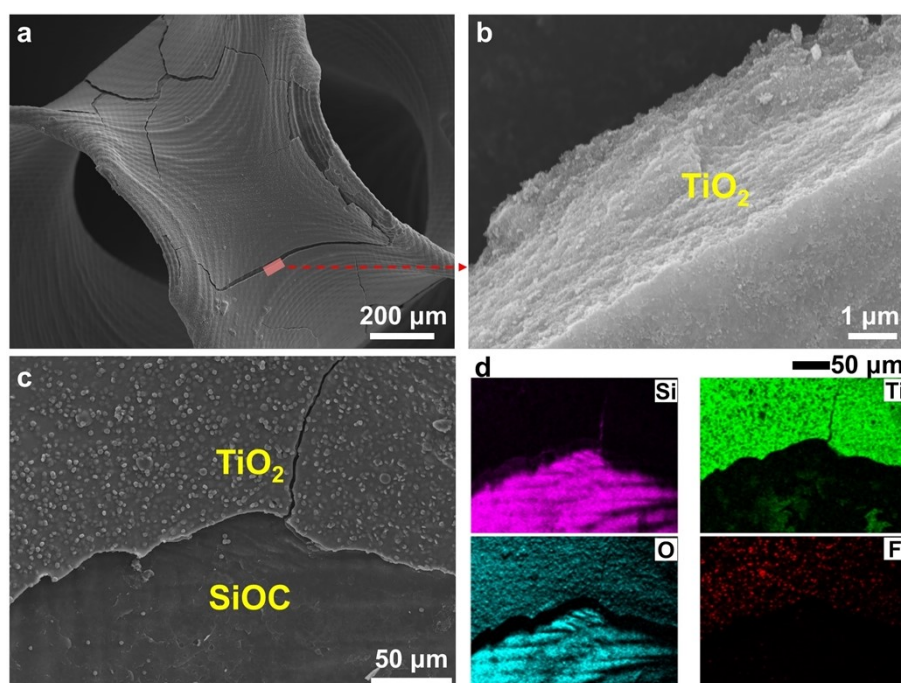


Fig. S6 For GGS110-2.0- z_{opt} M@SiOC specimens after testing at 500°C: (a) micromorphology at the EMW incident end; (b) the fracture surface of the MXene coating; (c-d) micromorphology of a region where the coating peeled-off from the SiOC substrate, and matching SEM-EDS elemental mapping images.

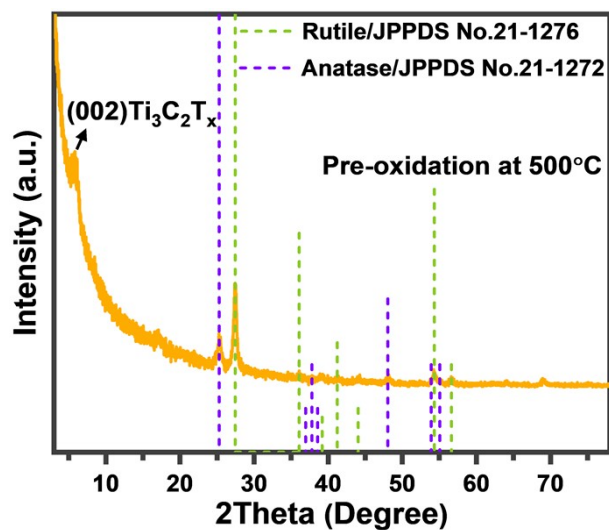


Fig. S7 XRD patterns of SC-MXene after pre-oxidizing treatment at 500°C in air.

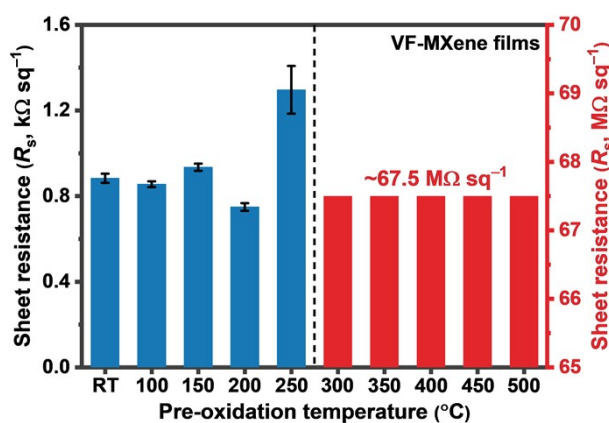


Fig. S8 The sheet resistance of SC-MXene films after the pre-oxidizing treatment at different temperatures in air.

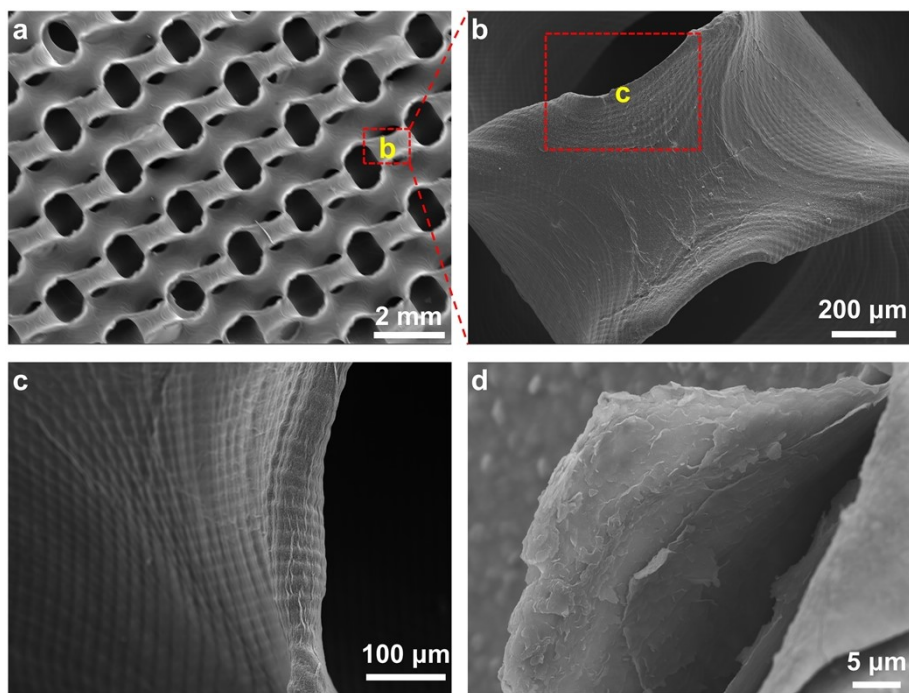


Fig. S9 For GGS110-2.0- z_{opt} M@SiOC specimens after IR testing carried out at temperatures from 100 to 450°C: (a-c) stepwise enlarged micromorphology at the EMW incident end; (d) the fracture surface of the SC-MXene coating.

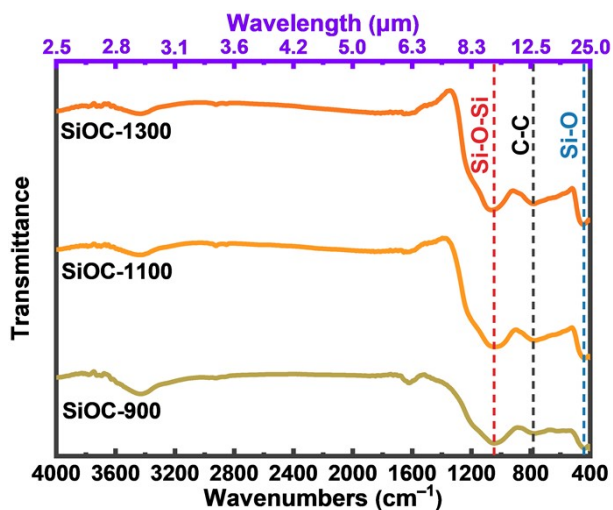


Fig. S10 Fourier transform infrared (FT-IR) spectra of SiOC pyrolyzed at different temperatures.

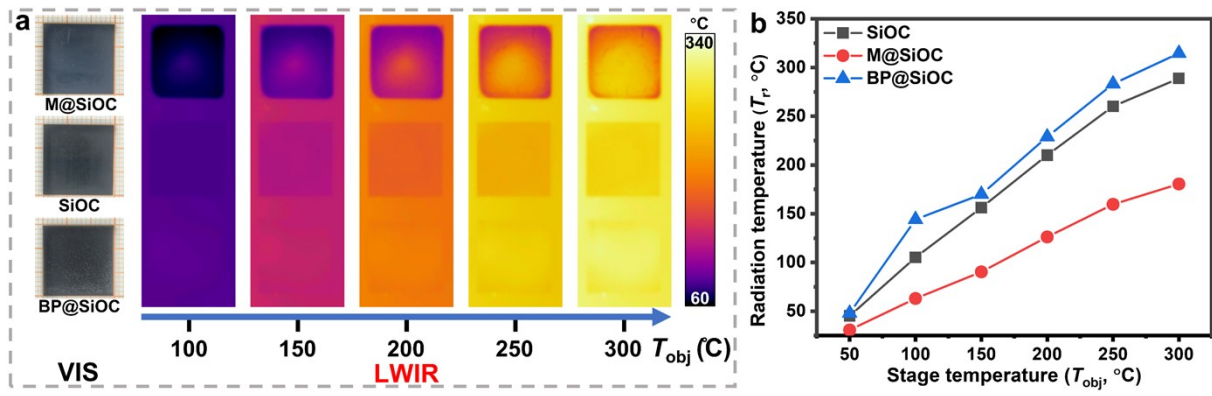


Fig. S11 (a) LWIR images and (b) measured radiation temperature (T_r) of bulk M@SiOC, SiOC, and reference BP@SiOC at different heating temperatures.

Supplemental Tables

Table S1. A comparison between data reported in published literature and in this work.

Refs.	Materials/structure	Thickness (mm)	MW camouflage		IR camouflage			Reflectance for 1.06- μm laser	VIS camouflage	Temperature intensity/work ing temperature ($^{\circ}\text{C}$)
			Absorptivity /frequency range (GHz)	Metal backplane dependence	MWIR	LWIR	Radiative cooling			
This work	GGs SiOC@MXene	7.18	>80%/(8.2-18.0) at RT; >86%/(8.2-18.0) at 500 $^{\circ}\text{C}$	No	$\epsilon = \sim 0.33$ at RT	78.5% signal reduction at 450 $^{\circ}\text{C}$	Yes	$\leq 7.3\%$	$\leq 7.5\%$	No/RT-450 $^{\circ}\text{C}$
16	Multilayered conductive carbon black (CCB)-filled PE composite films	17	$\sim 96.8\%$ /(2.35-18)	Yes	Yes	Yes	No	$\sim 6\%$	$\sim 95\%$	Yes/RT
17	Multilayer Ge/ZnS/Cu-ITO-Cu	2.2	>85.0%/(8-12)	Yes	53.4% signal reduction	13.0% signal reduction	Yes	N.A.	Tunability	Yes/RT-300 $^{\circ}\text{C}$
18	Hierarchical Au/ZnS/Quartz/FR4/Carbon/Cu metamaterials	~ 2.4	>99%/(8-12)	Yes	N.A.	95% signal reduction	Yes	No	No	Yes/RT
19	Metallodielectric metafilms	2.0	>90%/(8-12)	Yes	$\epsilon = 0.31$	$\epsilon = 0.31$	No	No	Transmittance of 68%	Yes/RT
20	Hierarchical Al/Si scattering surfaces	~ 7.4	>90%/(8-13)	Yes	N.A.	$\epsilon = 0.17$	No	N.A.	Tunability	Yes/ RT-100 $^{\circ}\text{C}$
21	Stacked Cu/Au /F4B metasurface	8.036	>90%/(3-8)	Yes	N.A.	$\epsilon = 0.2$	No	No	No	Yes/RT

22	Hierarchical Au/PET/Resistive film/Foam/Metal Metasurfaces	~11	>90%/(2.7-26)	Yes	$\varepsilon < 0.2$	$\varepsilon < 0.2$	No	< 15%	No	Yes/RT
23	Hierarchical Au/FR4/Cu/Resistive sheet metamaterial	3.517	>90%/(7-12.7)	Yes	~5%	~5%	No	$\leq 5\%$	No	Yes/RT
24	ITO films with different surface resistances	33	>80%/(5.4-9.4)	Yes	N.A.	~0.52	No	No	Transmittance of ~33%	Yes/RT
25	PI/PET/copper patches/ITO rings metasurface	2.26	> 90% /(8.2-16.0)	Yes	N.A.	$\varepsilon = 0.2$	No	No	No	Yes/RT
26	SiO ₂ (carbon) fiber skeleton multilaminate metastructure	5.6	>90%/(3.1-6.2) at 1000°C	Yes	N.A.	860°C reduction at T_{obj} 1200°C	No	N.A.	N.A.	Yes/RT-1000°C

Note: all displayed data are obtained from published experimental results, and N.A. means not available in the referred literature.

References

1. R. C. Zhu, J. F. Wang, S. Sui, Y. Y. Meng, T. S. Qiu, Y. X. Jia, X. F. Wang, Y. J. Han, M. D. Feng, L. Zheng and S. B. Qu, *Front. Phys.*, 2020, **8**.
2. R. Zhu, Z. Zhang, J. Wang, C. Xu, S. Sui, X. Wang, T. Liu, Y. Zhu, L. Zhang, J. Wang and S. Qu, *Opt. Express*, 2021, **29**, 20150-20159.
3. M. R. Lukatskaya, S. Kota, Z. F. Lin, M. Q. Zhao, N. Shpigel, M. D. Levi, J. Halim, P. L. Taberna, M. Barsoum, P. Simon and Y. Gogotsi, *Nat. Energy*, 2017, **2**.
4. A. Lipatov, M. Alhabeab, M. R. Lukatskaya, A. Boson, Y. Gogotsi and A. Sinitskii, *Adv. Electron. Mater.*, 2016, **2**.
5. M. Ghidui, M. R. Lukatskaya, M. Q. Zhao, Y. Gogotsi and M. W. Barsoum, *Nature*, 2014, **516**, 78-81.
6. L. Yao, W. Q. Yang, S. X. Zhou, H. Mei, L. F. Cheng and L. T. Zhang, *Carbon*, 2022, **196**, 961-971.
7. L. Yao, S. Zhou, L. Pan, H. Mei, Y. Li, K. G. Dassios, P. Colombo, L. Cheng and L. Zhang, *Adv. Funct. Mater.*, 2022, **33**.
8. L. Yang, T. Zhang, H. Zhou, S. C. Price, B. J. Wiley and W. You, *ACS Appl. Mater. Interfaces*, 2011, **3**, 4075-4084.
9. A. Sarycheva, A. Polemi, Y. Liu, K. Dandekar, B. Anasori and Y. Gogotsi, *Sci. Adv.*, 2018, **4**, eaau0920.
10. J. Lipton, J. A. Rohr, V. Dang, A. Goad, K. Maleski, F. Lavini, M. K. Han, E. H. R. Tsai, G. M. Weng, J. M. Kong, E. Riedo, Y. Gogotsi and A. D. Taylor, *Matter*, 2020, **3**, 546-557.
11. N. P. Avdelidis and A. Moropoulou, *Energ Buildings*, 2003, **35**, 663-667.
12. X. Wang, S. X. Huang, L. W. Deng, H. Luo, C. Li, Y. Xu, Y. Z. Yan and Z. X. Tang, *Physica E*, 2021, **127**.
13. D. Sharma and N. Jaggi, *Physica E*, 2017, **91**, 93-100.
14. J. Fatima, M. B. Tahir, A. Rehman, M. Sagir, M. Rafique, M. A. Assiri, M. Imran and M. Alzaid, *Mater Sci Eng B-Adv*, 2023, **289**, 116230.
15. Y. L. Bai, K. Zhou, N. Srikanth, J. H. L. Pang, X. D. He and R. G. Wang, *Rsc Adv.*, 2016, **6**, 35731-35739.

16. M. L. Li, B. Muneer, Z. X. Yi and Q. Zhu, *Adv. Opt. Mater.*, 2018, **6**.
17. H. Zhu, Q. Li, C. Tao, Y. Hong, Z. Xu, W. Shen, S. Kaur, P. Ghosh and M. Qiu, *Nat. Commun.*, 2021, **12**, 1805.
18. T. Kim, J. Y. Bae, N. Lee and H. H. Cho, *Adv. Funct. Mater.*, 2019, **29**.
19. R. C. Zhu, J. F. Wang, J. M. Jiang, C. L. Xu, C. Liu, Y. X. Jia, S. Sui, Z. T. Zhang, T. H. Liu, Z. T. Chu, J. Wang, T. J. Cui and S. B. Qu, *Photonics Res*, 2022, **10**, 1146-1156.
20. Y. Huang, Y. N. Zhu, B. Qin, Y. W. Zhou, R. Qin, P. Ghosh, M. Qiu and Q. Li, *Nanophotonics*, 2022, **11**, 3613-3622.
21. S. M. Zhong, W. Jiang, P. P. Xu, T. J. Liu, J. F. Huang and Y. G. Ma, *Appl. Phys. Lett.*, 2017, **110**.
22. X. D. Feng, M. B. Pu, F. Zhang, R. Pan, S. Wang, J. T. Gong, R. Y. Zhang, Y. H. Guo, X. Li, X. L. Ma and X. G. Luo, *Adv. Funct. Mater.*, 2022, **32**.
23. X. Feng, X. Xie, M. Pu, X. Ma, Y. Guo, X. Li and X. Luo, *Opt. Express*, 2020, **28**, 9445-9453.
24. S. Zhong, L. Wu, T. Liu, J. Huang, W. Jiang and Y. Ma, *Opt. Express*, 2018, **26**, 16466-16476.
25. C. Zhang, J. Yang, W. Yuan, J. Zhao, J. Y. Dai, T. C. Guo, J. Liang, G. Y. Xu, Q. Cheng and T. J. Cui, *J. Phys. D. Appl. Phys.*, 2017, **50**, 444002.
26. Z. M. An, Y. P. Li, X. G. Luo, Y. X. Huang, R. B. Zhang and D. N. Fang, *Matter*, 2022, **5**, 1937-1952.